Decoupling between strain localisation and the microstructural record revealed by in-situ strain measurements in polycrystalline ice

Marco A. Lopez-Sanchez*

Géosciences Montpellier – CNRS & Université de Montpellier, France
Present address: Dept. de Geología, Universidad de Oviedo, 33005, Oviedo, Spain

Thomas Chauve

Univ. Grenoble Alpes, CNRS, IRD, Grenoble INP, IGE, 38000 Grenoble, France

Maurine Montagnat

Univ. Grenoble Alpes, CNRS, IRD, Grenoble INP, IGE, 38000 Grenoble, France

Andrea Tommasi,

Géosciences Montpellier – CNRS & Université de Montpellier, France

**corresponding author: lopezmarco@uniovi.es*

Decoupling between strain localisation and the microstructural record revealed by in-situ strain measurements in polycrystalline ice

Lopez-Sanchez, Marco A.[1,2,*], Chauve, Thomas[3], Montagnat, Maurine[3], Tommasi, Andréa[1]

[1]*Géosciences Montpellier – CNRS & Université de Montpellier, Montpellier, France*
[2]*Present address: Dept. de Geología, Universidad de Oviedo, 33005, Oviedo, Spain*
[3] *Univ. Grenoble Alpes, CNRS, IRD, Grenoble INP, IGE, 38000 Grenoble, France*

**Corresponding author: e-mail: lopezmarco@uniovi.es*

Abstract

We explore the links between strain localisation and the evolution of the microstructure in ice Ih deforming by dislocation creep. Using digital image correlation (DIC), we monitored the evolution of the strain field in two coarse-grained columnar ice samples deformed by creep (uniaxial compression at constant load) at -7 °C and 0.5 MPa up to 9.5% bulk shortening. After a brief transient (<0.2% bulk strain), in which strain localises nearby grain boundaries, viscoplastic strain concentrates in a few narrow intracrystalline shear bands that eventually extend over multiple grains. A comparison of pre- and post-deformation crystal orientation maps shows that strain localisation in shear bands is mainly accommodated by basal glide without producing significant dislocation-related substructures. Severe dynamic recrystallization develops locally, at grain boundaries that act as barriers to dislocation motion, especially where transfer of basal shear is ineffective. These observations are compared to full-field simulations reproducing the initial microstructure and experimental setup, which predict the stress and strain rate fields for deformation entirely accommodated by dislocation glide on the know slip systems in ice. The present data indicate that during the deformation of coarse-grained ice Ih at high homologous temperatures: (1) recrystallization does not drive strain localisation but accommodates strain incompatibility and (2) large strains can be accommodated by unimpeded basal slip with no formation of dislocation substructures. Observation (2) implies that intragranular orientation gradients are unreliable gauges of viscoplastic strain intensity at the grain scale and that the proportion of dislocation types in subgrains does not gauge the relative contribution of different slip systems to deformation. To conclude, we discuss the implications of this study for the interpretation and modelling of deformation by dislocation creep in rocks.

keywords: Digital Image Correlation; Ice Ih; strain localisation; dynamic recrystallization; experimental deformation; viscoplastic anisotropy

Highlights

- Transient strain localisation at most grain boundaries occurs at strains <0.2%
- At higher strains, deformation occurs on a network of intracrystalline shear bands
- Shear bands associated with dislocation slip can leave no microstructural record
- Intragranular orientation gradients do not gauge strain intensity
- Recrystallization mainly accommodates grain-scale strain incompatibility

1. Introduction

Variations in crystal orientation and viscoplastic anisotropy result in highly heterogeneous stress and strain rate fields during the deformation of polycrystalline materials like ice, rocks, or metallic alloys. The heterogeneity in the stress and strain rate fields controls the evolution of the microstructure, which in turn modifies the mechanical response of the polycrystal both at the local and larger scales. Understanding the complex feedbacks between the evolution of the microstructure and stress and strain fields is thus essential to define accurate strain-dependent flow laws describing the mechanical behaviour of these materials. Deformation experiments that couple technologies to record (preferably in situ) the evolution of the strain field and microstructure at the polycrystal and grain scales are key to studying the links between these two variables. The evolution of the displacement and strain fields can be measured in situ by digital image correlation (DIC) of random speckle patterns deposited at the surface of the sample (Dong and Pan, 2017; Sutton et al., 2009), whereas the microstructure can be measured by optical or electron microscopy.

Due to its strong viscoplastic anisotropy, hexagonal (Ih) Ice is an ideal model material for probing the relations between local strain, intragranular misorientation, and dynamic recrystallization. Viscoplastic deformation in Ice Ih crystals occurs essentially by glide of dislocations with [1-120] Burger vectors on the basal plane (normal to the crystal [0001] or c-axis) since non-basal slip systems are at least 60 times harder to activate than the basal one (Duval et al., 1983; Weertman, 1983). Electron backscattered diffraction (EBSD) data on ice polycrystals show, however, that non-basal dislocations represent up to ~35% of the geometrically necessary dislocations delimiting subgrains (Chauve et al. 2017; Weikusat et al. 2017). The large resolved shear stresses required to activate the non-basal slip systems imply local high stress concentrations within the polycrystal.

Previous deformation studies using DIC on Ice Ih showed that the strain field is heterogeneous at both crystal and polycrystal scales. Uniaxial compression creep tests at -12°C, 0.5 MPa on columnar ice polycrystals documented strain localisation already in the transient creep stage (bulk strains $\leq 1\%$) (Grennerat et al., 2012). Local strains five to ten times larger than the bulk strain were measured in shear bands oriented at 30 to 60° to compression, with the highest strains nearby grain boundaries and triple junctions. Strain in individual grains does not correlate with the intensity of the bulk stress projected on the basal plane (i.e., the Schmid factor). This lack of correlation hints at a major effect of grain interactions on the stress and strain fields (Grennerat et al., 2012). DIC imaging of uniaxial compression creep tests in columnar ice at -7 and -10°C, 0.5 MPa to higher bulk strains showed that nucleation occurred mainly at triple junctions and along boundaries between grains with markedly different orientations, highlighting a relation between local strain incompatibility and dynamic recrystallization (Chauve et al., 2015; Piazolo et al., 2015). Grain-scale strain incompatibility also played an essential role in strain localisation at the brittle-plastic transition, where dynamic recrystallization and fracturing are coupled (Chauve et al., 2017b).

In the present study, we focus on how grain interactions and activation of different deformation mechanisms (intracrystalline slip, dynamic recrystallization, and formation of kinks) affect strain localisation and the evolution of the microstructure in coarse-grained polycrystalline materials deforming at high temperature. We performed compressional creep tests at high homologous temperatures at -7°C up to 9.3% bulk shortening on Ice Ih polycrystals composed of columnar centimetre-scale crystals. Using DIC, we tracked the evolution of the viscoplastic deformation field with a micrometric resolution over the entire surface normal to both the compression direction and the columnar structure of the ice. We monitored the changes in the microstructure ex-situ by mapping crystal orientations on thin sections cut parallel and as close as possible to the face analysed by DIC before and after deformation. These two sets of observations are compared to the predictions of a full-field FFT-based model reproducing the experimental set-up and initial microstructure of the samples, but in which deformation occurs only by dislocation glide. We then discuss the extrapolation of these results to other polycrystalline materials deforming by dislocation creep, focusing on their implications for the deformation of rocks.

2. Methods

We made polycrystalline columnar ice samples of 10×10×1.5 cm composed of ~65 to 75 columnar grains elongated normal to the square face of the sample, which is further referred to as the sample surface. The samples have thus a roughly 2D microstructure. The elaboration process is detailed in Grennerat et al. (2012). The area of the grain sections on the sample surface varies both within and among samples, but most grains are centimetric (Figs 1 and 2). Grain boundaries lie nearly perpendicular to the sample surface in most cases. The large grain size favours dislocation creep relative to diffusion creep and grain boundary sliding. The columnar microstructure facilitates the study of interactions between grains with different orientations and the detection of dynamically recrystallized grains. However, due to the limited number of grains, the samples are not representative volume elements, and their mechanical response may be strongly conditioned by a few coarse grains at key positions in the aggregate, as for example the coarse grain that occupies more than half of the central part of sample A (Fig. 1).

We performed uniaxial creep tests (initial stress of 0.5 MPa) under unconfined conditions (room pressure) where the load is applied perpendicular to the columnar structure of the grains using an in-house dead-weight rig at -7 ºC (0.97 T_m, where T_m is the melting temperature). Axial stress decreased slightly over time from 0.5 MPa to 0.49 MPa (for sample A deformed to a total bulk shortening of 3.1%) or 0.48 MPa (for sample B deformed to a total bulk shortening of 9.5%, Fig. 3a) due to a slight increase in the cross-sectional area of the samples. Instantaneous strain rates during the experiments ranged from 3×10^{-7} to 9×10^{-7} s^{-1} (Fig. 3b, c). Bulk strain (ε) at a given time was calculated by two different methods: (1) measuring the change in sample length ($l - l_0$) in the shortening direction directly on the image sequence based on the displacement of the press trays and using $\varepsilon(\%) = 100 \times |(l - l_0) \div l_0|$ and (2) averaging (median) the ε_{yy} component, y being the compression direction, over the full strain field estimated from digital image correlation.

For digital image correlation, a random speckle pattern was created on the sample surface by scratching-abrading the surface with sandpaper and then applying shoe polish with a brush to create high-contrast grey intensity gradients (for details on the procedure see Grennerat et al., 2012). The evolution of the displacement and the strain field during the experiments were measured using the free open-source Digital Image Correlation Engine (DICe) tool (https://github.com/dicengine/dice) v2.0 from Sandia National Laboratories (Turner, 2015). Details on the methods and parameters used are provided in Table 1, Appendix A, and as metadata in the Supplementary material. Raw image resolutions were 17.26 μm/pixel (sample A) and 17.98 μm/pixel (sample B); detailed image acquisition setup and procedures are described in the Supplementary material. The optimal subset size was set at 35 × 35 pixels using the autocorrelation approach (Sutton et al., 2009). For an optimal result, step and virtual strain gauge (VSG) sizes were set at 12 (~1/3 of the subset size) and 24 pixels, respectively (International Digital Image Correlation Society et al., 2018). The step size corresponds physically to ~210 μm (VSG ~420 μm) and the maximum displacement resolution estimated was of ±6–7 μm for the x-direction (horizontal) and ±12–15 μm for the y-direction (vertical). The evolution of the strain field is presented as the Von Mises 2D equivalent strain ε_{eq} field

$$\varepsilon_{eq} = \sqrt{\frac{2}{3}\left(\varepsilon_{xx}^2 + \varepsilon_{yy}^2 + 2\varepsilon_{xy}^2\right)} \qquad (1)$$

The maximum equivalent strain resolution expected is $\pm5.7\times10^{-4}$ (sample B) and $\pm7.3\times10^{-4}$ (sample A), respectively. Strain field maps are presented as (1) incremental equivalent strain estimated over a 10 min creep interval normalized to the interval median equivalent strain, or as (2) finite (cumulative) equivalent strain. For reference, the bulk (longitudinal) shortening $\varepsilon(\%)$ is indicated in all strain field maps.

Table 1. Parameters and methods used to perform incremental DIC

Parameter/Method	Value
Initialization	feature matching
Optimization	gradient-based and simplex
Interpolation	keys cubic
Subset size	35 × 35 pixels (~612 × 612 μm)
Step size	12 pixels (~210 μm)
VSG size	24 × 24 pixels
Camera	Nikon D850 45.7 Mpx BSI CMOS sensor
Optics	Low-distortion Tamron SP Macro 1:1 lens
Image FOV	87-92 mm (height)
Image scale	~17.5 μm/pixel
Imaging rate	10 min
Exposure time	1/10 s

To characterize the evolution of the microstructure, we mapped the orientation of c-axes (azimuth θ and colatitude ϕ) before and after deformation on thin sections (~0.4 mm thick) cut parallel and as close as possible to the observation surface using the Automatic Ice Texture Analyser (AITA), which provides an angular resolution of ~3° (Peternell et al., 2011; Wilson et al., 2003). Pre- and post-deformation maps have spatial resolutions of 50 and 20 μm, respectively. Orientation data treatment, maps, and pole figures were made using the AITAToolbox (https://mecaiceige.gricad-pages.univ-grenoble-alpes.fr/tools/documentations/AITA-book/docs/intro.html).

As Ice Ih deforms essentially by dislocation glide on the basal plane, the theoretical capacity of a grain to deform when subjected to axial compression can be approximated by the Schmid factor of the basal slip system using:

$$m_s = sin\phi\ sin\theta\ (\ 1 - sin^2\phi\ sin^2\theta)^{\frac{1}{2}} \quad (2)$$

A Schmid factor of 0.5 characterises grains with c-axes at 45° from the compression direction, leading to maximum resolved shear stresses on the basal plane, whereas a zero value implies c-axes parallel or perpendicular to the compression direction, leading to null resolved shear stresses on the basal plane. However, in strongly anisotropic polycrystals such as ice, the Schmid factor calculated using the macroscopic imposed stress is an unreliable measure of a crystal's ability to deform because grain interactions may produce local stresses that differ strongly in intensity and orientation relative to the macroscopic imposed stress (Grennerat et al., 2012). Comparison of the "macroscopic" Schmid factor with the actual strain of the grain provides therefore an estimate of the deviation of the local stresses relative to the macroscopic one.

Lastly, we performed full-field micro-macro simulations based on the pre-deformed microstructure of the samples using the CraFT code (Moulinec and Suquet, 1998). CraFT models crystal plasticity using an algorithm based on the discrete Fast Fourier Transform (FFT). It predicts the evolution of strain and stress fields in response to an imposed deformation for a prescribed crystal plasticity constitutive law and an initial microstructure by minimizing the average local work rate under strain compatibility and stress equilibrium constraints. For simulating the deformation of Ice Ih, we used the elasto-viscoplastic law described in Suquet et al. (2012), which considers three slip systems: basal, prismatic, and pyramidal, strongly favouring basal slip. This constitutive law has been validated by comparison with experimental data at low strain (Grennerat et al., 2012; Piazolo et al., 2015). Since the simulation ignores changes in the microstructure (i.e. recrystallization), it can only reliably predict stress and strain fields before the development of recrystallization, i.e. below 1% bulk shortening (Chauve et al., 2015). Grain boundaries only represent contrasts in crystallographic orientation between crystals with no specific physical properties or behaviours and thus no possibility of sliding or opening. The predicted strain and stress fields will therefore be used as likely predictors of recrystallization occurrence, through the work (the

product of strain and stress). The initial microstructure of the sample surface was discretized at a 0.15 mm·pixel^{-1} step size giving respectively 533 × 600 (sample A) and 571 × 578 (sample B) Fourier points. Creep conditions equivalent to the experimental ones were applied up to a 1% bulk shortening, but the simulations have periodic boundary conditions, which differ from the stress-free lateral surfaces in the experimental setup. The effect of such an approximation was estimated to be negligible except on the very edges of the sample by Grennerat et al. (2012).

3. Results

3.1 Microstructural evolution

Sample A

The evolution of the microstructure of sample A is well illustrated by the analysis of two coarse grains, denoted as grains #1 and #2 in figure 1a, which accommodated most strain in this sample and had contrasted behaviours. Grain #1, in the centre of the sample, had initially a rather homogeneous orientation with its basal planes at ~78° to the bulk compression direction. Grain #2, in the lower-left section of the sample, shows well-defined subgrain boundaries delimiting domains with basal planes at 0° to 33° to the bulk compression direction before deformation. Both grains had low to moderate (<0.25) initial Schmid factors indicating unfavourable crystal orientations to trigger basal slip in response to the imposed macroscopic stress (Fig 1d).

After a bulk shortening of 3.1%, grain #1 preserved weak intragranular orientation gradients despite a marked change in shape. Grain #2 shows less pronounced change in shape, but strong orientation gradients in the form of closely spaced kink bands and subgrain boundaries (Figs. 1a, b, c). Many grain boundaries display millimetre-sized grains formed by dynamic recrystallization (Fig. 1b, c), but severe dynamic recrystallization is limited to the grain boundary between grains #1 and #2, and those on the right side of grain #1 (Fig. 1c, g).

Sample B

Sample B had a more homogeneous initial microstructure and a wider range of crystal orientations than sample A (Fig. 2). The upper right corner of sample B is composed of grains less than 1 cm wide, but more than 2/3 of the sample is composed of coarse columnar grains (Grains #1 to #7) with similar sizes (~3-6 grains across the sample height) (Fig. 2a). Most coarse grains had their basal planes initially oblique to the imposed compression (Fig. 2a, e), resulting in moderate to high (>0.3) Schmid factors for basal glide (Fig. 2d). Sample B also had a few grains with basal planes parallel to the sample surface (dark hues in the orientation maps) and low Schmid factors (e.g., grain #2 in Fig. 2a). Low Schmid factors also predominated among the smaller grains in the upper right corner of the sample (Fig. 2e).

After a bulk shortening of 9.5%, most coarse grains display an increase in the intragranular misorientation (Fig. 2b, c). As in sample A, the intragranular misorientation varies strongly among grains. For example, grains #1 and #6 show smooth orientation gradients, whereas grains #4 and #7 display sharp orientation gradients delimited by kink bands and closely-spaced subgrains. The higher bulk shortening resulted in more extensive dynamic recrystallization than in sample A. Dynamic recrystallization developed mostly: (i) within grain #2 and its neighbours, (ii) along the boundary segment between grains #4 and #5, and (iii) to the right of grains #5 and #7 (Fig 2b, c). Comparison of crystal orientations before and after deformation reveals some dispersion of the original orientations due to intragranular distortion and recrystallization, but no major grain reorientations (Fig. 2e).

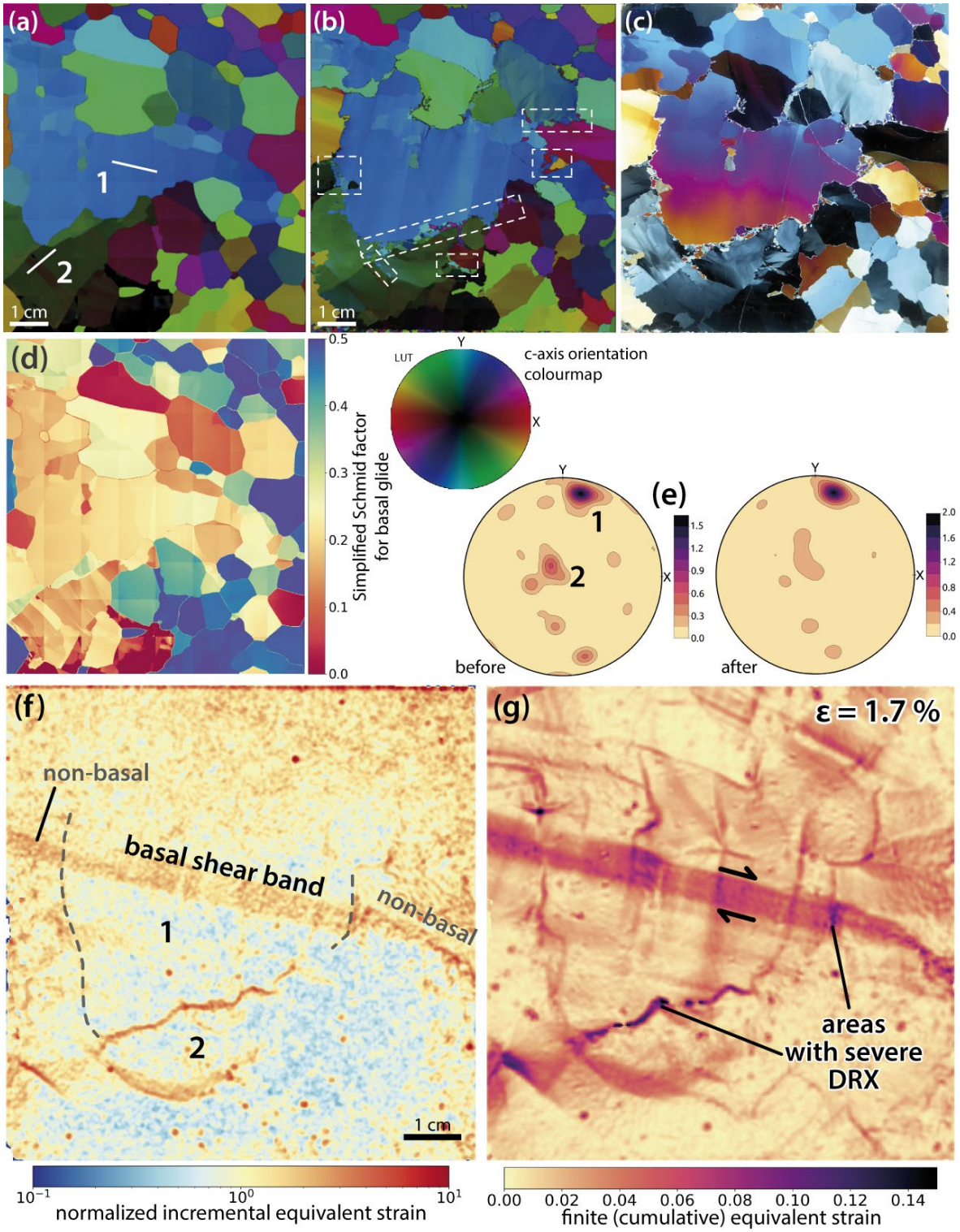

Figure 1. Microstructure, Schmid factor for basal glide, pre- and post-deformation CPO maps, and strain field at 1.7% bulk strain for sample A. The compression direction is vertical in all images. **(a, b)** Pre- and post-deformation (3.1% bulk shortening) c-axis orientation maps. The projection of the basal planes onto the sample surface in the numbered grains is indicated by white lines in (a). Recrystallized areas are indicated by rectangles with dashed lines. **(c)** Post-deformation cross-polarized light image; the gentle colour gradient from top to bottom is a bias due to a smooth change in thickness of the thin section. **(d)** Schmid factor map for basal glide according to initial crystal orientations. **(e)** Pre- and post-deformation contoured c-axis pole figures with orientations of grains #1 and #2 indicated. Upper hemisphere equal-area projections. **(f)** Incremental Von Mises (2D) equivalent strain normalized to the median at 1.7% of bulk longitudinal strain. Blue and red areas are strained below and above the average respectively. Basal and non-basal shear bands are indicated. Incremental strain is estimated every 10 minutes of creep. **(g)** Finite (cumulative) Von Mises 2D equivalent strain at 1.7% of bulk strain.

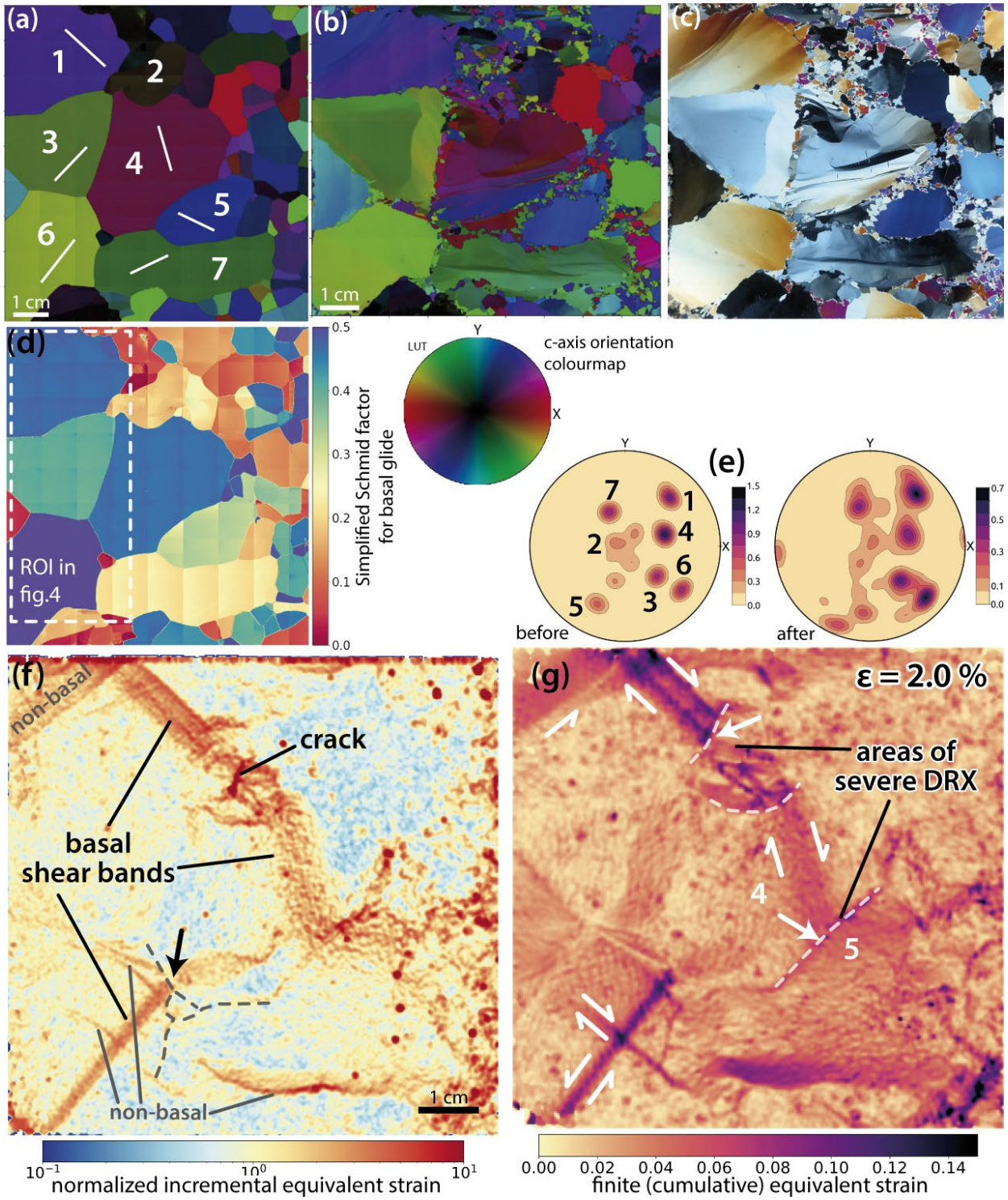

Figure 2. Microstructure, Schmid factor for basal glide, pre- and post-deformation CPO maps, and strain field at 2.0% bulk strain for sample A. The compression direction is vertical in all images. **(a, b)** Pre- and post-deformation (9.5% bulk shortening) c-axis orientation maps. The projection of the basal planes onto the sample surface in the numbered grains is indicated by white lines in (a). **(c)** Post-deformation cross-polarized light image. **(d)** Schmid factor map for basal glide according to initial crystal orientations. Note that grains #1, #4, #6 have high Schmid factors (c-axis at ~45–73° to the compression normal), whereas grain #2 and #7 have moderate to low Schmid factors. The square indicates the region of interest (ROI) for which DIC could be performed until the end of the experiment (cf. figure 4). **(e)** Pre- and post-deformation contoured c-axis pole figures with orientations. Upper hemisphere equal-area projections. **(f)** Normalized incremental Von Mises (2D) equivalent strain at 2.0% of bulk strain. Basal and non-basal shear bands, the location of the crack produced at 1.4% of shortening and a few selected grain boundaries (dashed lines) are indicated. The black arrow indicates an example of slip transfer across a grain boundary (from grain #6 to #4). **(g)** Finite

(cumulative) Von Mises 2D equivalent strain at 2.0% of bulk strain. The white dashed lines and arrows indicate a few selected grain boundaries that act as barriers to the dislocation motion in the basal shear bands, leading to the development of severe dynamic recrystallization in the neighbouring grain.

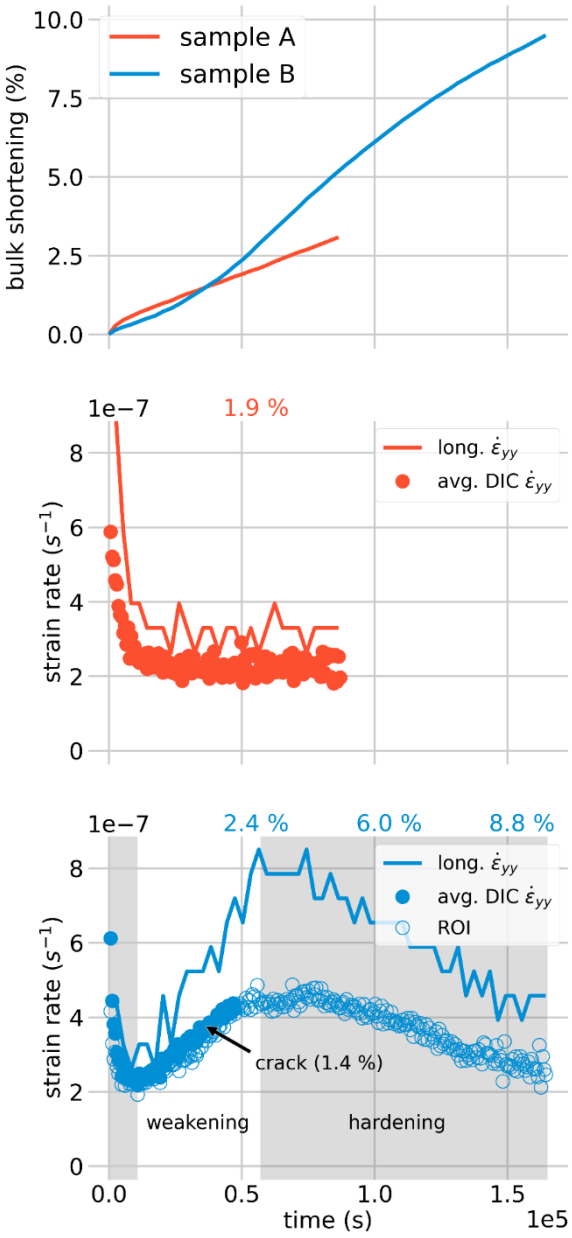

Figure 3. Evolution of bulk strain and strain rate over time. For comparison, the time scale is the same in all plots. **(a)** Creep curves for samples A and B. Bulk shortening is the finite engineering strain parallel to the shortening axis. **(b)** Evolution of strain rate with time in sample A determined via the longitudinal change in sample length (full line) and as the variation of the median of strain in the vertical direction $\dot{\varepsilon}_{yy}$ determined by DIC (markers). **(c)** Evolution of strain rate with time in sample B (symbols as in (b)). Due to the degradation of the speckle pattern quality with time, DIC-derived strain rates were estimated over the whole area only up to 2.4 %. For higher strains, DIC analysis was estimated on a region of interest (ROI, *cf.* figure 2d) where the speckle pattern preserved a good quality (hollow markers). After a short primary creep (~0.4%), sample B underwent an accelerated creep stage (weakening) up to ~2.9% and a deceleration creep stage (hardening) to completion at 9.5%. The different creep stages are highlighted by shaded areas. The equivalence between time and finite longitudinal strain is given at selected points for both samples at the top (in colour). The time at which the crack occurs in sample B is also indicated.

3.2 Macroscopic mechanical behaviour and the mean-field strain evolution from DIC

Sample A, shortened up to 3.1%, showed a primary creep stage characterized by a sharp decrease in the strain rate down to ~3×10^{-7} s^{-1} at ~0.9 % bulk shortening. Then, the strain rate remained constant (steady state) until the end of the experiment (Fig. 3a, b). The evolution of the median strain rate ($\dot{\varepsilon}_{yy}$) estimated from DIC follows a similar trend (Fig. 3b), validating the DIC strain field measurements up to 3.1%.

The macroscopic mechanical evolution of sample B, shortened up to 9.5%, is markedly different (Fig. 3a, c). Sample B displayed a faster primary creep stage with a decrease in strain rate down to ~2.5×10^{-7} s^{-1} at ~0.4% of bulk shortening. However, primary creep was not followed by steady-state but by an increase in strain rate (softening) up to ~8×10^{-7} s^{-1} at ~2.9% bulk shortening and then by a decrease in strain rate (hardening) until the end of the experiment down to a strain rate of ~4.6×10^{-7} s^{-1} at 9.5% bulk shortening. The variation with time of the median strain rate ($\dot{\varepsilon}_{yy}$) estimated from DIC follows a similar trend than the bulk longitudinal strain even when the DIC strain is estimated over a small region that retained an acceptable quality speckle pattern (dashed box in Fig. 2d), thus validating the DIC data in this region up to 9.5%.

3.3 Strain field evolution from DIC

Both samples showed an initial transient stage in which strain localised nearby grain boundaries (at a scale of hundreds of microns or smaller). In this stage, incremental equivalent strains 5 to 10 times higher than the average occurred near virtually all grain boundaries (Figs. 4, 5 and 6). In-plane rotation maps indicate that this strain localisation along grain boundaries often has a simple shear component (Fig. 4). Analysis of the DIC data for this early stage in sample B also reveals intragranular shear bands that propagate from triple junctions (arrows in Fig. 4). Strain localisation vanished along most grain boundaries at a longitudinal shortening of less than 0.2 % (i.e. at primary creep) (Figs. 5 and 6; see also movies A2 and B2 in Supplementary Material) in both samples. The transient stage in sample B was followed by a short period of almost homogeneous deformation up to a bulk strain of ~0.4% (Fig. 6 and movie B2 for a full sequence). DIC data show strain localised in a few shear bands, with apparent widths ranging from 1 to 8 mm, which grew until they coalesced to form an almost continuous system crosscutting the entire sample (Figs. 1, 2, 5 and 6). The exact evolution of the strain field differs, however, between the two samples.

Strain localisation: Sample A

As previously described, almost 1/3 of sample A was composed of two very coarse grains (#1 and #2) with low to moderate (<0.25) Schmid factors. DIC-derived strain maps indicate that these grains accommodated most of the imposed deformation. Strain localisation started early, at 0.1% bulk shortening, at two sites. The first site (grey arrows in Fig. 5) is the lower segment of the grain boundary between grains #1 and #2, which was the only grain boundary preserving strain localisation at the end of the initial transient stage (Figs. 1f, g and 5). Strain continued to accumulate at this interface until the end of the experiment, but its intensity varied in time and space along the grain boundary and the strain localisation along this grain boundary decreased during the experiment (Fig 5; see movie A2 in Supplementary Material). Most dynamic recrystallization in this sample occurred along this grain boundary (Fig. 1b, c). Strain localisation propagated from this grain boundary into grain #2 forming a slightly curved non-basal band with a diffuse end (Figs. 1f, g and 5). A shear band with a similar orientation also developed in grain #2 from the left edge of the sample and linked to the grain boundary via a more diffuse strain localisation band. Strain localisation in the non-basal bands was accompanied by the formation of subgrains, kinks, and, in the curved one, dynamic recrystallization (Fig 1c).

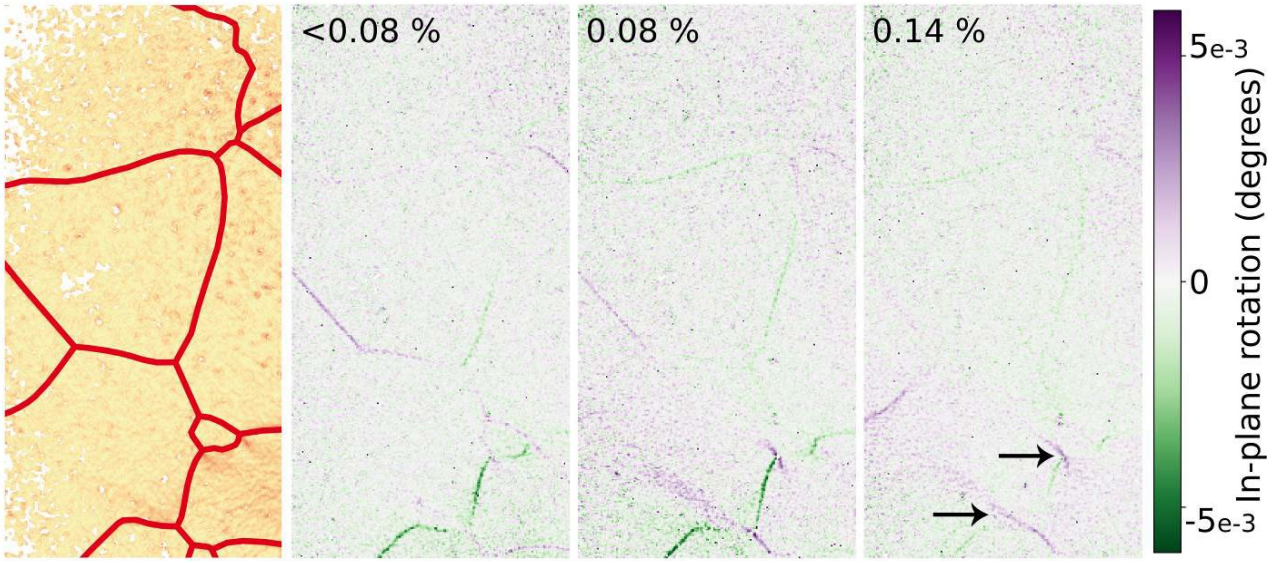

Figure 4. Example of the initial transient deformation stage in the region of interest of sample B. On the left, equivalent strain map at <0.08% bulk longitudinal shortening with delineated initial grain boundaries for reference. The sequence shows how (shear) strain localised and delocalised quickly at grain boundaries using in-plane rotation maps; purple and green colours indicate clockwise and counter-clockwise shear senses, respectively. The complete initial transient stage for both samples is presented in the Supplementary material.

In parallel, a ~7 mm wide shear band developed within grain #1 parallel to its basal plane at a high angle (77.5°) to the imposed shortening (Figs. 1f, g and 5). Already at 0.28% of bulk shortening, this shear band crosscut the entire grain and propagated into the neighbouring grains (~1.5–4 mm wide), affecting the entire sample width. The orientation of the shear band parallel to the basal plane of crystal #1 indicates that most deformation was accommodated by basal slip despite the moderate Schmid factor of the grain (~0.2, see Fig. 1d). The shear band is on average thinner in the neighbouring grains where it is not parallel to the basal plane. Transient (at bulk shortenings between 0.28-1%) strain localisation occurred at the intersection between the band and the boundary of grain #1 on the right, which is another site with severe development of dynamic recrystallization (cf. Figs. 1f, g and 5). Strain concentration at this boundary decreased with the propagation of the shear band into the neighbouring grains up to the free surface of the sample (see movie A2 in Supplementary Material). Within grain #1, this shear band produced neither dynamic recrystallization nor significant dislocation substructures, remaining invisible in the optical image and the crystallographic orientation map (cf. Figs. 1cb, c vs. f, g). From ~1.8% bulk shortening onwards, a slightly thinner basal shear band developed in this same grain spaced from the first one by ~1 cm. It did not propagate into neighbouring grains but produced some strain localisation and limited recrystallization at its interception with the boundary of grain #1 on the left (see movie A2 in Supplementary Material).

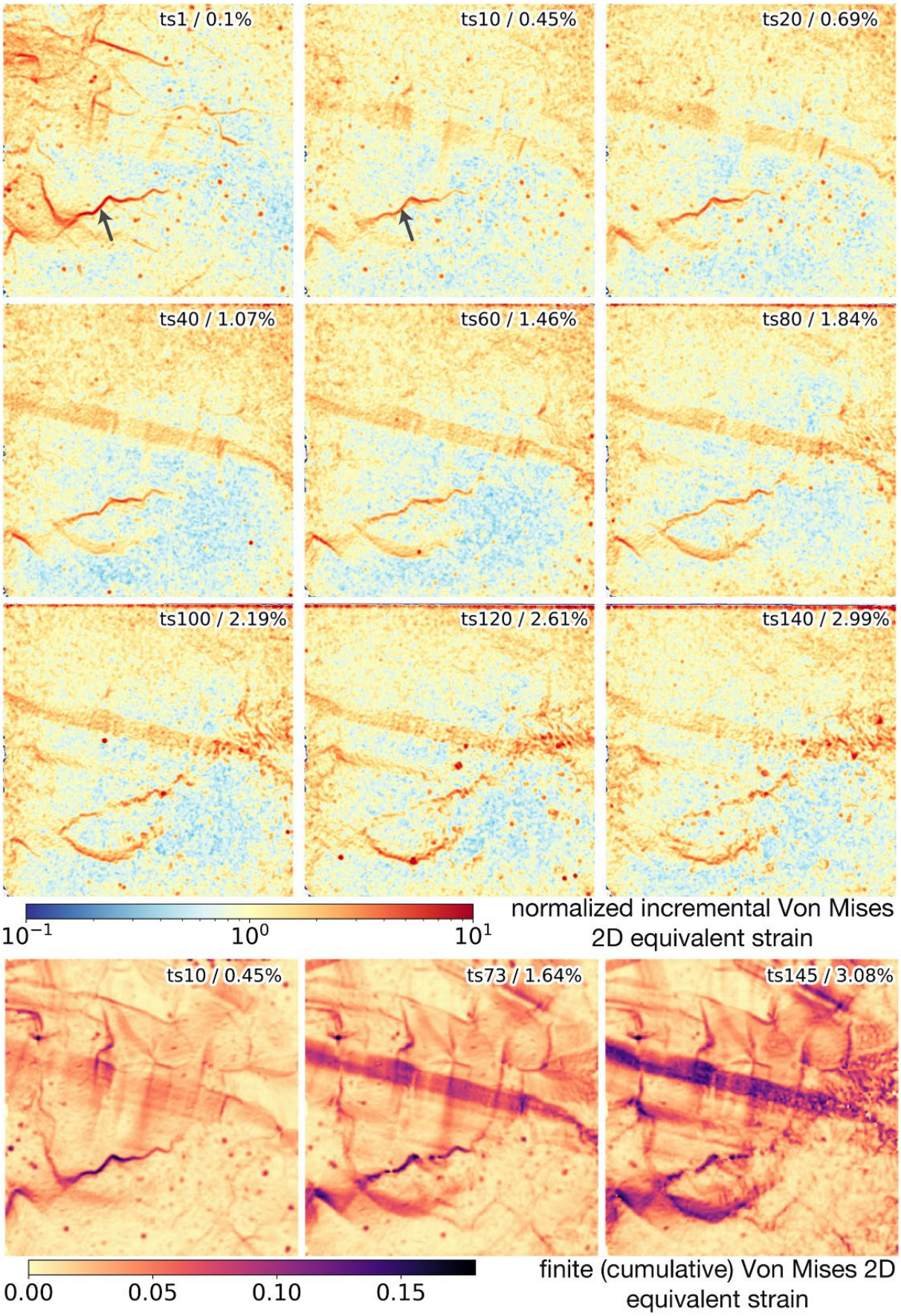

Figure 5. Selected frames of the sequence of incremental (estimated every 10 minutes of creep) and finite equivalent 2D strain evolution of sample A (for the complete sequence see movie A2 in Supplementary material). For reference, the time step (*ts*), i.e., the image number within the correlation sequence, and percentage of bulk longitudinal shortening are indicated in the top left of each image.

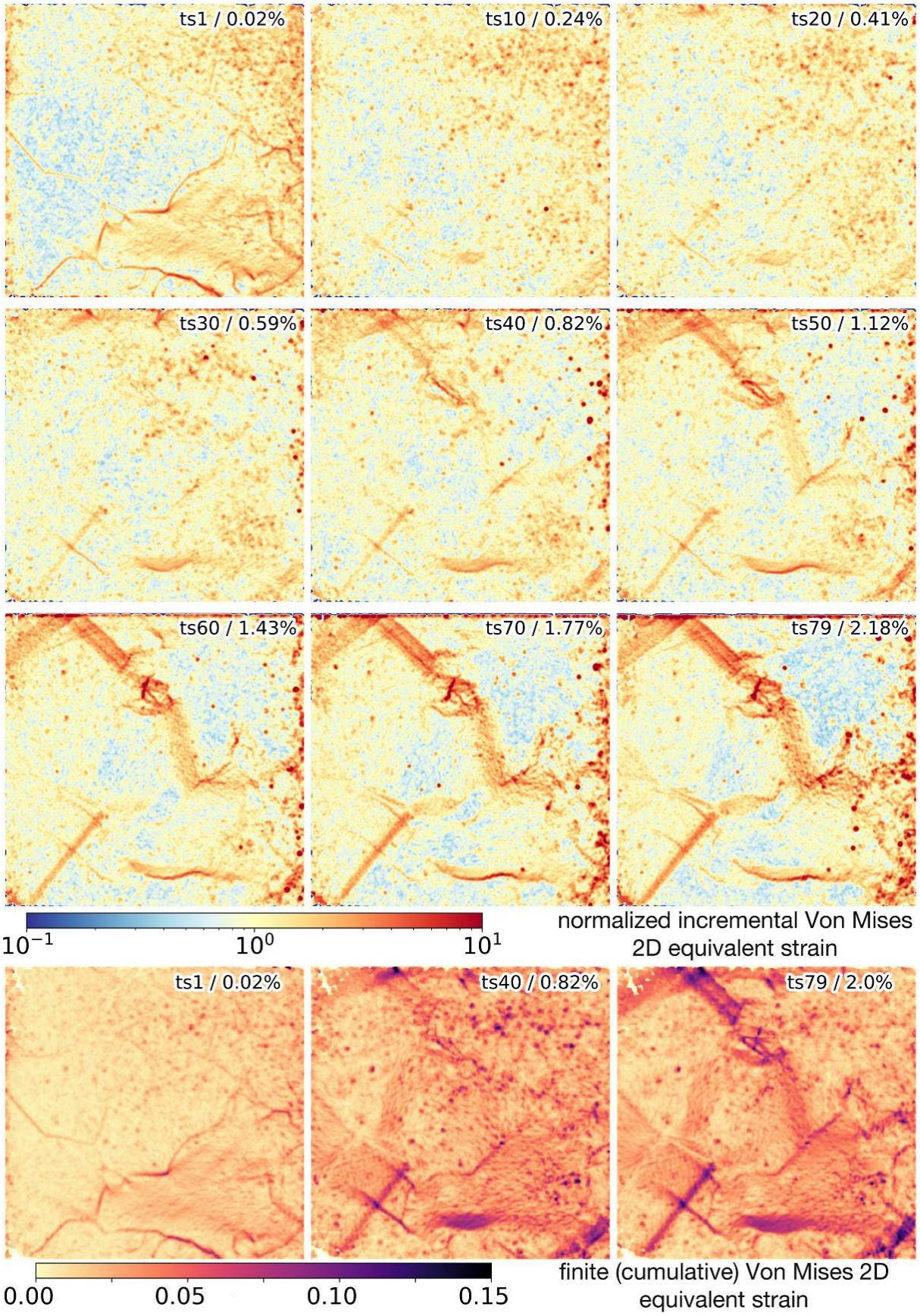

Figure 6. Selected frames of the sequence of incremental (estimated every 10 minutes of creep) and finite equivalent 2D strain evolution of sample B (for the complete sequence see movie B2 in Supplementary material). For reference, the time step (*ts*), i.e., the image number within the correlation sequence, and percentage of bulk longitudinal shortening are indicated in the top left of each image.

Strain localisation: Sample B

After the initial transient stage, DIC data show that strain in sample B was mostly accommodated in a network of mm-wide (apparent thicknesses vary between 3 and 7.5 mm) intragranular shear bands oblique (13° to 45°) to the compression (Figs. 2f, g and 6). Macroscopically, the development of this shear band network corresponds to the weakening stage evidenced by the increase in strain rate over time (Fig. 3c). Shear bands formed mainly in coarse grains with high Schmid factors (>0.4) following the orientation of the basal plane, specifically in grains #1, #4 and #6 (Figs. 2a vs f, g). However, a few shear bands do not follow basal planes (Figs. 2c, f, g). Grains #1 and #6 also display conjugate shear bands perpendicular to the basal planes associated with subgrain boundaries (Fig. 2f). Grain #7 displays strong strain localisation linked to a kink band. In grain #6, the non-basal shear band nucleated already in the transient stage from a triple junction (Fig. 4). The non-basal shear bands are thinner (in grain #6) or less marked (in grain #1) than the basal ones.

The DIC sequence shows that strain localisation started at multiple sites and the shear bands propagated unevenly across the sample. The formation of shear bands started as early as 0.14% of bulk shortening in the lower part of the sample (Fig. 4). The basal shear band affecting grain #6 propagated from the triple junction between grains #6, #4, and a tiny grain with a very low Schmid factor value located between grains #4, #6, and #7 and evolved fast crosscutting the entire grain #6 at a bulk shortening ~0.7% (Fig. 6 and movie B2 in Supplementary material). Strain localisation became progressively stronger within it and at bulk shortenings ~1.4% this shear band propagated into grain #4 towards the other shear band system (Fig. 6).

The best-developed shear bands in sample B propagated with a basal orientation from the top of the sample into grain #1 at a bulk shortening of 0.73% (see movie B2), continued into grain #2 as a non-basal deformation band with a fuzzy strain distribution, and propagated into grain #4 as a basal shear band at a bulk shortening of ~0.8% (Figs. 2f, g and 6; see also movie B2). The deformation band stalled at the grain boundary between grains #4 and #5, producing a marked strain concentration along the grain boundary (Figs. 2f, g and 6). Lastly, diffuse build-up of strain in grain #5 and its neighbours, which were subjected to extensive recrystallization, connected the shear band system to the right edge of the sample, producing a strain localisation network that crosscut the whole sample. Within grain #2, the propagation of the shear band was accompanied by the development of a crack normal to the shear band direction at a bulk shortening of 1.4% and extensive dynamic recrystallization (Figs. 1f, 5 and movie B2).

3.4 Links between the strain field and microstructures

In both samples, basal-slip shear bands produced no visible microstructural changes in polarised optical images or crystallographic orientation maps, whereas non-basal shear bands left a clear signature in the microstructure in the form of strong orientation gradients, kink bands, or dynamic recrystallization (Figs. 1 and 2 and movies A2 and B2 in Supplementary material). In sample B, grains #1, #4 and #6, deformed mainly through basal-slip shear bands, underwent a notable change in shape during deformation consistent with the high strain they accumulated. However, this change in shape can only be assessed because the initial stage is known. In contrast, although many non-basal strain localisation bands are linked with kink bands or closely spaced subgrain walls, these microstructures are not systematically linked with significant long-lasting strain localisation (cf. kink bands in grain #4 of sample B, Fig. 2).

There is a correlation between the sites where the shear bands propagation stalled and the generation of severe dynamic recrystallization. Three sites in sample B display severe recrystallization (Fig. 2b, c vs g). One is the boundary between grains #4 and #5, where the basal shear band in grain #4 stalled due to the strong misorientation between the two grains. The other corresponds to grain #2, a grain with an exceptionally low Schmid factor that serves as a strain transfer zone between the basal shear bands in grains #1 and #4. The development of a small crack in grain #2 at ~1.4% bulk shortening indicates that it supported high local stresses even if the bulk sample was weakening, as indicated by the increase in bulk

strain rate (Fig. 3c). The last severe recrystallization site in sample B links the lower left termination of the shear band, characterized by diffuse deformation in grain #5, to the sample edge.

Comparison of the initial Schmid factor for basal slip and the average finite strain from DIC for a few coarse grains from both samples shows that the two parameters are uncorrelated (Fig. 7). This explicitly indicates that the local stress field strongly deviates from the macroscopic one due to interactions between neighbouring grains.

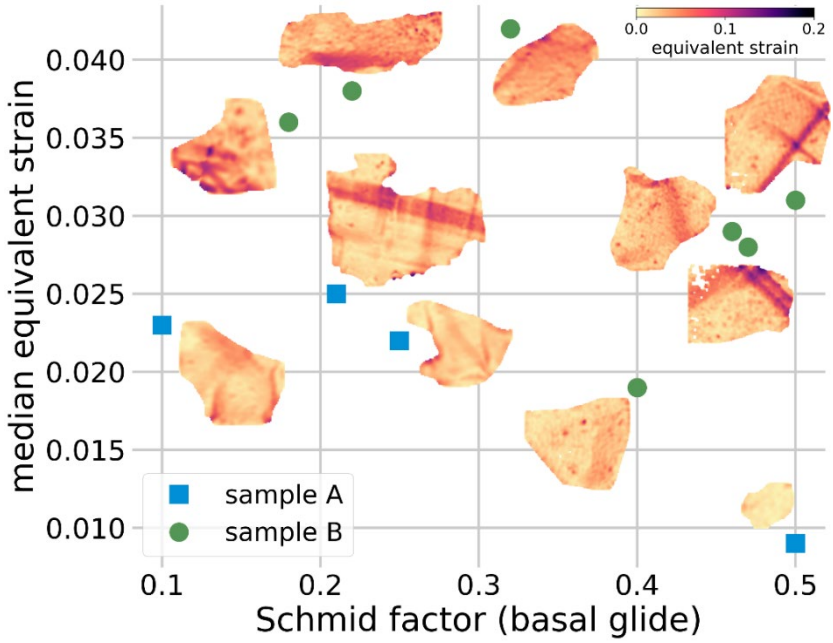

Figure 7. Schmid factor vs median equivalent strain in selected grains of samples A and B at 2% bulk longitudinal shortening illustrating the lack of correlation between the two variables. Grains are not represented at the same scale. Colour maps indicate cumulative equivalent strain at 2% bulk shortening.

4. Discussion

4.1 Experimental data

The most striking observation when comparing the evolution of the strain field and that of the microstructure in both samples is the decoupling between finite strain and the development of microstructures linked to the accumulation of geometrically necessary dislocations, such as crystal lattice distortion, recrystallization, or the development of kink bands. The most effective strain localisation, well recorded by DIC, occurred through intracrystalline shear bands parallel to the basal planes of the crystals and this deformation produced hardly any lattice distortion (intragranular misorientation) or dynamic recrystallization within the grains but a marked change in shape. This strain at grain scale can only be quantified by in situ observational techniques such as DIC or if the initial state is known, which is rarely the case in nature.

Our results agree with the large body of evidence that creep deformation in single-grain and polycrystalline ice proceeds mainly by dislocation glide on basal planes (Duval et al., 1983; Weertman, 1983). Most of the deformation accommodated by basal slip remains undetectable to observations based on intracrystalline misorientation (e.g. AITA, EBSD) resulting from the accumulation of geometrically necessary dislocations (GNDs). This observation solves the paradox that despite a deformation mainly accommodated by basal dislocation glide, non-basal dislocations contribute up to 35-40% of the total intracrystalline misorientation in Ice Ih polycrystals (as measured with high spatial resolution cryo-

EBSD mapping and X-ray Laue diffraction, Chauve et al. 2017; Weikusat et al. 2017). These observations also imply that estimating the (geometrically necessary) dislocations density within a crystal based on misorientation proxies – such as the grain orientation spread (GOS), the kernel average misorientation (KAM), or the average misorientation between subgrains – does not gauge the total viscoplastic strain at the grain scale. Therefore, caution must be applied when using such proxies to estimate the strain intensity at local scales.

Dynamic recrystallization occurred mainly nearby grain boundaries and triple junctions, as in previous studies (Chauve et al., 2015; Piazolo et al., 2015), but it was best developed along grain boundaries with misorientations that hindered the transfer of dislocation motion associated with basal slip between grains (e.g. at the interface between grains #4 and #5 in Fig. 2). Accordingly, the intensity of recrystallization is related to the deformation incompatibility between neighbouring grains caused by a local concentration of stress and strain. This means that, under the experimental conditions tested, dynamic recrystallization is a consequence rather than a driver of deformation localisation, insofar as it relaxes the deformation incompatibility between neighbouring grains. In other words, dynamic recrystallization is not the seed of strain localisation in the early stages of ice deformation.

The analysis of the evolution of the mechanical behaviour of the samples is hindered because samples are not representative volume elements (they are composed of a limited number of coarse grains). Still, some qualitative conclusions can be drawn based on the evolution of the strain field documented by DIC. Sample A developed a strain localisation network crossing the entire sample already at 0.45% bulk shortening (Fig. 6) and shows a simple mechanical evolution, where primary creep (hardening) is followed by steady-state deformation (Fig. 5). In sample B, the development of a strain localisation network crossing the entire sample is slower, completing at ~1% bulk shortening (Fig. 7). The development of the strain localisation network might be related to the marked weakening that started at the end of the primary creep (Fig. 5). The progressive hardening characterizing sample B up to ≥3% bulk shortening (Fig. 7) can be linked to the observed decrease in strain localisation in the shear band network (see full DIC sequence for ROI of sample B in Supplementary material). However, the small area over which it has been possible to map the strain field at large bulk strains due to the speckle deterioration makes it difficult to analyse the causes of this behaviour change.

4.2 Comparison between experimental observations and simulations

As expected, comparison between the full-field simulations and experimental observations reveals a general but not one-to-one agreement between the predicted and observed strain distribution (Fig. 8). The agreement is satisfactory for sample A, where the simulation predicts well the intragranular basal shear band that crosscuts grain #1 and accommodates most of the strain in the sample. For sample B, although the general strain distribution at the sample scale is correctly forecasted, the shear bands are not. The comparison between observations and simulations suggests that dynamic recrystallization developed preferentially in sites where the work was high, hinting a link between both. Higher than average work sites did not always display severe recrystallization at the end of the experiment as many developed kinks or subgrains. Besides, the strong recrystallization around grain #5 in sample B does not coincide with high work sites in the simulation.

The mismatch between simulations and observations are attributed to the fact that processes that change the microstructure such as the formation of kinks, subgrains, or recrystallization cannot be reproduced in the simulations. We stopped the simulations at 0.5% bulk strain to alleviate this limitation. Yet, DIC data show evidence of the formation of some kink or tilt bands at these low strains (Figs. 6 and 7). Since all microstructural changes occurring during deformation affect the future development of the strain field, this explains the larger discrepancy between observations and simulations for sample B, which was subjected to larger strain and thus to stronger changes in the microstructure. For example, analysis of the evolution of the strain field with time for sample B (Fig. 6) shows that the shear band in grain #4 developed after the strain concentration associated with recrystallization in grain #2. Thus, despite the lack of one-to-one agreement, the comparison with the simulation suggest that a higher than average

local work rate is necessary to trigger severe microstructural changes such as dynamic recrystallization or kinking.

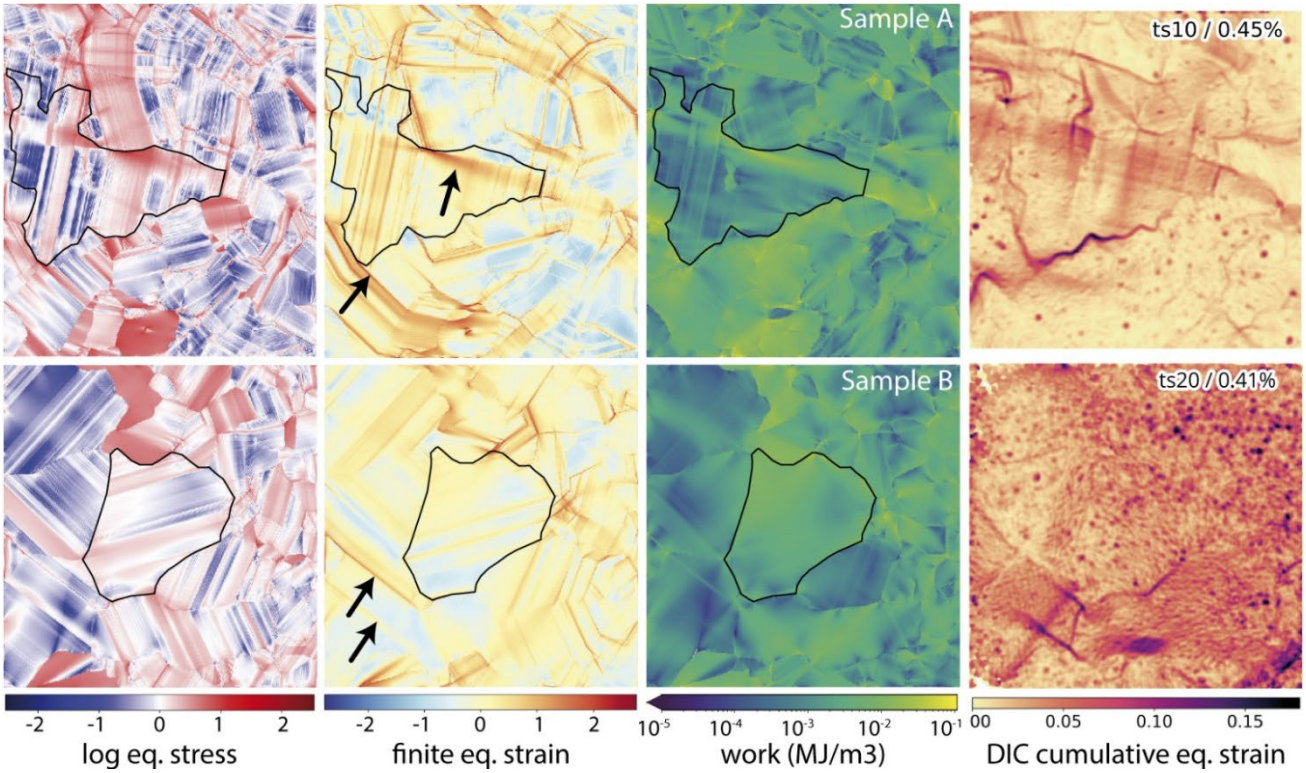

Figure 8. Full-field simulations: normalized equivalent stress, equivalent strain, and plastic work fields at a bulk longitudinal shortening of 0.5% (compression direction is vertical), and finite equivalent strain maps derived from DIC data at similar bulk shortenings (right-hand column). Two grains are delineated onto the simulated fields to facilitate comparison with DIC data. Arrows on the simulated strain maps indicate sites where strain localisation is also present in the experimental data.

4.3 Extrapolation to rocks (and metals) deforming by dislocation creep

Simply put, the present study provides evidence of decoupling between finite strain and microstructural imprint (evidenced by misorientation gradients and recrystallization) at the sample and grain scales. Recent studies correlating high-resolution (nm scale) DIC and crystal orientation mapping through EBSD during deformation experiments in the dislocation creep regime also recorded decoupling between strain intensity and development of intragranular misorientations in magnesium, which as ice Ih is a hexagonal material and deforms mainly via basal slip and twinning (Orozco-Caballero et al. 2017), and face-centred cubic nickel alloys, which activate multiple slip systems for any crystal orientation (Harte et al. 2020). The latter indicate that this decoupling is not only limited to materials with a strong viscoplastic anisotropy that tend to deform by single slip.

Due to the need to deform rock samples at high temperatures and under confining pressure to avoid fracturing (except for rock salt, but halite is a cubic material more akin to metals than to silicate minerals), in situ DIC experiments are unfeasible. Despite this experimental limitation, several lines of evidence indicate that this decoupling phenomenon is extensible to common rocks that deform predominantly by dislocation creep. Evidence is stronger for mantle rocks, which are essentially composed of olivine (>60%), a highly anisotropic orthorhombic mineral having only three independent slip systems with contrasted strengths (Tommasi et al. 2000). Experiments on olivine crystals oriented to activate only the [100](010) slip system, which has the lowest critical resolved shear stresses under most natural and experimental deformation conditions, recorded very low misorientation gradients despite substantial shear (Tielke et al., 2019). Further evidence that large strains are decoupled from strong intragranular disorientations at the grain scale is the predominance of strongly elongated olivine porphyroclasts perfectly oriented for single-slip deformation on the easy [100](010) system both in

olivine polycrystals deformed in torsion (Bystricky et al . 2000) and in natural peridotites deformed under various conditions (Falus et al., 2011). Extreme elongation (aspect ratios up to 20:1) without the development of strong intracrystalline misorientations or recrystallization was also documented for orthopyroxenes in peridotite mylonites (Frets et al., 2014). Another indirect evidence of this decoupling phenomenon in natural and experimentally deformed peridotites is the discrepancy between the relative activity of the slip systems in olivine deduced from the bulk crystal preferred orientation, which usually indicates dominant activation of the [100](010) sliding system and the rotation axes that accommodate intragranular misorientations, which often indicate a dominant activity of the [100](001) and [001](100) systems (Bystricky et al . 2000; Falus et al., 2011; Lopez-Sanchez et al. 2021; Soustelle et al., 2010). In crustal rocks, evidence is less clear due to their usual polymineralic nature, which results in further heterogeneity in stress at the grain scale, several deformation mechanisms acting in parallel, and because deformation is often accompanied by chemical reactions. However, quartz mylonite formed under low greenschist facies often displays monocrystalline quartz ribbons composed of crystals well oriented to deform by dislocation glide on the basal plane (the dominant slip system in quartz at low temperature) with rather low intracrystalline misorientations (e.g., Tommasi et al. 1994; Pauli et al., 1996).

In summary, we propose that the decoupling between strain intensity and the development of intragranular misorientations is generalizable to all rocks deforming by dislocation creep. As for ice, this means that caution must be applied when using misorientation-based proxies to estimate the strain intensity at local scales. Even if a relationship may exist between the bulk strain and the average misorientation over representative elementary volumes (e.g., Hughes et al., 1998; Pennock and Drury, 2003), microstructural parameters (e.g. grain size, CPO) and intensive variables such as temperature do affect this relation, hindering the establishment of a reliable universal approximation.

A second implication of this study is that in the early stages of deformation dynamic recrystallization may assist in localising or delocalising strain at the grain scale but is not a primary controlling factor of strain localisation. It is rather a process that accommodates local strain incompatibility. A similar relationship between recrystallisation and local strain incompatibility has been documented in experimentally and naturally deformed coarse-grained peridotites with incipient dynamic recrystallization. In these rocks, recrystallisation developed preferentially in olivine grains that are well-oriented to deform by dislocation glide in low-strength slip systems in contact with olivine grains in "hard" orientations, which remain almost undeformed, or pyroxenes, which are stiffer than olivine (Bickert et al., 2021; Lopez-Sanchez et al., 2021). A similar phenomenon was documented in polymineralic rocks with higher strength contrasts such as granites (e.g., Holyoke and Tullis, 2006). A secondary outcome is that since dynamic recrystallization is triggered by strain incompatibility and linked with local stress concentrations (and high work in the simulations), palaeopiezo(watt)metric relationships based on recrystallized grain size should be used with caution, particularly in the early stages of deformation when recrystallised volumes are low, as they may overestimate stresses or work rates.

5. Conclusion

Under the experimental condition tested, the combination of DIC and crystal orientation mapping reveals that deformation in Ice Ih tends to localise in intracrystalline shear bands dominated by basal glide, which eventually spread across multiple grains by direct transmission or, in neighbouring grains poorly oriented for basal slip, by recrystallisation, kinking or formation of non-basal glide shear bands. The association of DIC and microstructural data provides clear evidence that unimpeded basal glide may accommodate large strains at the grain scale without leaving any imprint on the final microstructure (orientation gradients, subgrains, or kinks). In contrast, when it cannot be accommodated by basal glide, deformation leaves a measurable footprint in optical images and orientation maps in the shape of subgrains (delimited by basal and non-basal dislocations, e.g., Chauve et al. 2017a), kink bands, or dynamic recrystallization. This decoupling between strain intensity and the development of dislocation substructures in ice Ih implies that misorientation-based proxies are unreliable gauges of both the viscoplastic strain intensity at the grain scale and the relative contribution of different slip systems to the

bulk deformation. The present results also highlight the role of local strain incompatibility (and associated stress rise) in triggering dynamic recrystallization. Under the tested experimental conditions (coarse grains, high temperature, moderate stress), our data show that grain size reduction by dynamic recrystallization is a consequence rather than a driver of strain localisation.

Similar experiments on metallic alloys and microstructural data in the mantle and, to a lesser extent, crustal rocks indicate that decoupling between strain intensity and the development of intragranular microstructures is a typical feature of deformation of crystalline materials by dislocation creep, best expressed in coarse-grained metallic alloys or rocks composed of highly anisotropic crystals, such as mantle rocks. This calls for a general warning on the limits of misorientation-based proxies to gauge the cumulative plastic deformation at the grain scale or smaller or the relative contributions of the different slip systems to the bulk strain. This also calls for further testing of the common assumption of a simple relation between average intragranular misorientation and finite strain at the polycrystal and larger scales. The heterogeneity in the strain and stress fields documented here results from the viscoplastic anisotropy of ice Ih. Thus, any rock composed of highly anisotropic minerals, such as olivine, quartz at low temperature, or micas will exhibit a similar or higher degree of heterogeneity in stress and strain, with dynamic recrystallization preferentially triggered at high work rate sites. Accordingly, paleopiezometry or paleowattmetry should be used with care. The grounds for extending the conclusion that grain size reduction by dynamic recrystallization is a consequence rather than a driver of strain localisation are less robust. Yet, given the similarity of deformation processes in ice Ih and other rock-forming minerals, it is expected that in the initial stages of deformation, before grain-boundary accommodated deformation becomes dominant, the same cause-and-effect relationship holds for rocks.

Acknowledgements. This work was supported by a postdoctoral fellowship co-funded by the European Union and the Government of the Principality of Asturias (Spain) [grant number ACA17-32] within the Marie Skłodowska-Curie COFUND Actions FP7 to MALS and by the European Research Council (ERC) under the European Union's Horizon 2020 Research and Innovation programme [grant agreement No 882450 – ERC RhEoVOLUTION]. We thank two anonymous reviewers for comments that helped to focus and improve the manuscript. All supplementary material related to this study will be published upon acceptance.

Appendix A. Digital image correlation data treatment

DICe software provides different algorithms for digital image correlation. We used the *feature matching* algorithm for the initialization, a *gradient-based* method for optimization, and the *Keys cubic* method (Keys, 1981) for interpolation (see metadata in Supplementary material). For some specific sequences of interest, we also used the simplex algorithm for optimization, as it produces a better coverage at the cost of a much longer time to correlate the images. The formulation used to compute the displacement and strain full-fields from digital image sequences is detailed in Turner (2018, 2016). During image correlation, subsets with the sum of a square of subset intensity gradients (SSSIG) proxy (Pan et al., 2008) above 150 were discarded, this ultimately produces a few missing values within the strain maps, but correlation coverage remains above 99% in all cases.

To visualize variations in the strain intensity, we used the Von Mises 2D equivalent strain (see equation 1) and in-plane rotation maps that plot the rotational component of the 2D strain. DIC strain estimate can include elastic and plastic components without distinction. We assumed that the elastic part for a stress of 0.5 MPa in ice is negligible, i.e., with Young's modulus of 9.1 GPa which implies $\varepsilon_{elastic} \ll \varepsilon_{plastic}$, and thus all the measured strain is considered plastic/viscoplastic. The quality of the DIC solution and the floor noise (maximum expected precision) for the displacement and strain (VSG) gauges were calculated by comparing the images acquired in the undeformed state under the same

environmental conditions and using the same displacement and strain parameters to analyse the deformed sequence.

Samples suffered from speckle quality degradation with time, including speckle tearing at high finite strains in sample B (see movie B1 in Supplementary Material). These issues were overcome by: (1) using incremental image correlation, which complied with one of the central goals of the study that was to track the evolution of the incremental strain with time, (2) focusing the study on regions where the random speckle pattern was better preserved over time, and (3) reconstructing the maps using convolution (interpolation) algorithms to replace missing data and remove noise based on neighbour's values. For convolution, we used the Python Astropy module v4.2.1 (Robitaille et al., 2013) with a Gaussian kernel (see Supplementary Material). We also performed finite correlations for specific deformation stages and individual grains. In these cases, we increased the subset and the VSG size to 45 x 45 pixels and the step size to 15 pixels to improve coverage and strain accuracy at the cost of losing spatial resolution. General post-processing procedures can be consulted in https://github.com/marcoalopez/Jupyter4DICe.

Out-of-plane specimen deflections were checked after deformation. For sample A (bulk shortening of 3.1 % after 24h:10 min), most of the surface remained flat excepting a small area in the upper left corner related to the development of a shear band. For sample B (shortening of 9.5% after 45h:50 min), the final surface was wavy with out-of-plane displacements of up to a few mm (see Supplementary Material). Based on sample A, we expect that the surface remained fairly flat up to ~3% bulk shortening. Yet, strain maps for the entire surface of sample B were limited to a maximum bulk strain of 2% due to speckle degradation.

References

Bickert, M., Cannat, M., Tommasi, A., Jammes, S., Lavier, L., 2021. Strain Localisation in the Root of Detachment Faults at a Melt-Starved Mid-Ocean Ridge: A Microstructural Study of Abyssal Peridotites From the Southwest Indian Ridge. Geochemistry, Geophysics, Geosystems 22, e2020GC009434. https://doi.org/10.1029/2020GC009434

Bystricky, M., Kunze, K., Burlini, L., Burg, J.-P., 2000. High Shear Strain of Olivine Aggregates: Rheological and Seismic Consequences. Science 290, 1564–1567. https://doi.org/10.1126/science.290.5496.1564

Chauve, T, Montagnat, M., Lachaud, C., Georges, D., Vacher, P., 2017b. Strain field evolution at the ductile-to-brittle transition: a case study on ice. Solid Earth 8, 943–953. https://doi.org/10.5194/se-8-943-2017

Chauve, T., Montagnat, M., Piazolo, S., Journaux, B., Wheeler, J., Barou, F., Mainprice, D., Tommasi, A., 2017a. Non-basal dislocations should be accounted for in simulating ice mass flow. Earth Planet. Sci. Lett. 473, 247–255. https://doi.org/10.1016/j.epsl.2017.06.020

Chauve, T., Montagnat, M., Vacher, P., 2015. Strain field evolution during dynamic recrystallization nucleation; A case study on ice. Acta Mater. 101, 116–124. https://doi.org/10.1016/j.actamat.2015.08.033

Dong, Y.L., Pan, B., 2017. A Review of Speckle Pattern Fabrication and Assessment for Digital Image Correlation. Exp. Mech. 57, 1161–1181. https://doi.org/10.1007/s11340-017-0283-1

Duval, P., Ashby, M.F., Anderman, I., 1983. Rate-controlling processes in the creep of polycrystalline ice. J. Phys. Chem. 87, 4066–4074. https://doi.org/10.1021/j100244a014

Falus, G., Tommasi, A., Soustelle, V., 2011. The effect of dynamic recrystallization on olivine crystal preferred orientations in mantle xenoliths deformed under varied stress conditions. J. Struct. Geol. 33, 1528–1540. https://doi.org/10.1016/j.jsg.2011.09.010

Frets, E.C., Tommasi, A., Garrido, C.J., Vauchez, A., Mainprice, D., Targuisti, K., Amri, I., 2014. The Beni Bousera Peridotite (Rif Belt, Morocco): an Oblique-slip Low-angle Shear Zone Thinning the Subcontinental Mantle Lithosphere. J. Petrol. 55, 283–313. https://doi.org/10.1093/petrology/egt067

Grennerat, F., Montagnat, M., Castelnau, O., Vacher, P., Moulinec, H., Suquet, P., Duval, P., 2012. Experimental characterization of the intragranular strain field in columnar ice during transient creep. Acta Mater. 60, 3655–3666. https://doi.org/10.1016/j.actamat.2012.03.025

Harte, A., Atkinson, M., Preuss, M., Quinta da Fonseca, J., 2020. A statistical study of the relationship between plastic strain and lattice misorientation on the surface of a deformed Ni-based superalloy. Acta Mater. 195, 555–570. https://doi.org/10.1016/j.actamat.2020.05.029

Holyoke, C.W., Tullis, J., 2006. Mechanisms of weak phase interconnection and the effects of phase strength contrast on fabric development. Journal of Structural Geology 28, 621–640. https://doi.org/10.1016/j.jsg.2006.01.008

Hughes, D.A., Chrzan, D.C., Liu, Q., Hansen, N., 1998. Scaling of Misorientation Angle Distributions. Phys. Rev. Lett. 81, 4664–4667. https://doi.org/10.1103/PhysRevLett.81.4664

International Digital Image Correlation Society, Jones, E.M.C., Iadicola, M.A. (Eds.), 2018. A Good Practices Guide for Digital Image Correlation. https://doi.org/10.32720/idics/gpg.ed1

Keys, R., 1981. Cubic convolution interpolation for digital image processing. IEEE Trans. Acoust. Speech Signal Process. 29, 1153–1160. https://doi.org/10.1109/TASSP.1981.1163711

Lopez-Sanchez, M.A., Tommasi, A., Ismail, W.B., Barou, F., 2021. Dynamic recrystallization by subgrain rotation in olivine revealed by electron backscatter diffraction. Tectonophysics 815, 228916. https://doi.org/10.1016/j.tecto.2021.228916

Moulinec, H., Suquet, P., 1998. A numerical method for computing the overall response of nonlinear composites with complex microstructure. Comput. Methods Appl. Mech. Eng. 157, 69–94. https://doi.org/10.1016/S0045-7825(97)00218-1

Orozco-Caballero, A., Lunt, D., Robson, J.D., Quinta da Fonseca, J., 2017. How magnesium accommodates local deformation incompatibility: A high-resolution digital image correlation study. Acta Materialia 133, 367–379. https://doi.org/10.1016/j.actamat.2017.05.040

Pan, B., Xie, H., Wang, Zhaoyang, Qian, K., Wang, Zhiyong, 2008. Study on subset size selection in digital image correlation for speckle patterns. Opt. Express 16, 7037–7048. https://doi.org/10.1364/OE.16.007037

Pauli, C., Schmid, S.M., Heilbronner, R.P., 1996. Fabric domains in quartz mylonites: localised three dimensional analysis of microstructure and texture. Journal of Structural Geology 18, 1183–1203. https://doi.org/10.1016/S0191-8141(96)00017-X

Pennock, G.M., Drury, M.R., 2005. Low-angle subgrain misorientations in deformed NaCl. J. Microsc. 217, 130–137. https://doi.org/10.1111/j.1365-2818.2005.01410.x

Peternell, M., Russell-Head, D. s., Wilson, C. j. l., 2011. A technique for recording polycrystalline structure and orientation during in situ deformation cycles of rock analogues using an automated fabric analyser. J. Microsc. 242, 181–188. https://doi.org/10.1111/j.1365-2818.2010.03456.x

Piazolo, S., Montagnat, M., Grennerat, F., Moulinec, H., Wheeler, J., 2015. Effect of local stress heterogeneities on dislocation fields: Examples from transient creep in polycrystalline ice. Acta Mater. 90, 303–309. https://doi.org/10.1016/j.actamat.2015.02.046

Robitaille, T.P., Tollerud, E.J., Greenfield, P., Droettboom, M., Bray, E., Aldcroft, T., Davis, M., Ginsburg, A., Price-Whelan, A.M., Kerzendorf, W.E., Conley, A., Crighton, N., Barbary, K., Muna, D., Ferguson, H., Grollier, F., Parikh, M.M., Nair, P.H., Günther, H.M., Deil, C., Woillez, J., Conseil, S., Kramer, R., Turner, J.E.H., Singer, L., Fox, R., Weaver, B.A., Zabalza, V., Edwards, Z.I., Bostroem, K.A., Burke, D.J., Casey, A.R., Crawford, S.M., Dencheva, N., Ely, J., Jenness, T., Labrie, K., Lim, P.L., Pierfederici, F., Pontzen, A., Ptak, A., Refsdal, B., Servillat, M., Streicher, O., 2013. Astropy: A community Python package for astronomy. Astron. Astrophys. 558, A33. https://doi.org/10.1051/0004-6361/201322068

Soustelle, V., Tommasi, A., Demouchy, S., Ionov, D.A., 2010. Deformation and fluid-rock interaction in the supra-subduction mantle: Microstructures and water contents in peridotite xenoliths from the Avacha volcano, Kamchatka. J. Petrol. 51. https://doi.org/10.1093/petrology/egp085

Suquet, P., Moulinec, H., Castelnau, O., Montagnat, M., Lahellec, N., Grennerat, F., Duval, P., Brenner, R., 2012. Multi-scale modeling of the mechanical behavior of polycrystalline ice under transient creep. Procedia IUTAM, IUTAM Symposium on Linking Scales in Computations: From Microstructure to Macro-scale Properties 3, 76–90. https://doi.org/10.1016/j.piutam.2012.03.006

Sutton, M.A., Orteu, J.-J., Scheirer, Hubert, 2009. Image Correlation for Shape, Motion and Deformation Measurements, 1st ed. Springer, Boston, MA.

Tielke, J., Mecklenburgh, J., Mariani, E., Wheeler, J., 2019. The Influence of Water on the Strength of Olivine Dislocation Slip Systems. J. Geophys. Res. Solid Earth 124, 6542–6559. https://doi.org/10.1029/2019JB017436

Tommasi, A., Vauchez, A., Femandes, L.A.D., Porcher, C.C., 1994. Magma-assisted strain localisation in an orogen-parallel transcurrent shear zone of southern Brazil. Tectonics 13, 421–437. https://doi.org/10.1029/93TC03319

Turner, D. Z., 2018. An overview of the virtual strain gauge formulation in DICe (No. Sandia Report, SAND2018-5463 R).

Turner, D. Z., 2016. An overview of the gradient-based local DIC formulation for motion estimation in DICe (No. Sandia Report, SAND2016-7360 R).

Turner, D. Z., 2015. Digital Image Correlation Engine (DICe) Reference Manual, (No. Sandia Report, SAND2015-10606 O).

Weertman, J., 1983. Creep Deformation of Ice. Annu. Rev. Earth Planet. Sci. 11, 215–240. https://doi.org/10.1146/annurev.ea.11.050183.001243

Weikusat, I., Kuiper, E.-J.N., Pennock, G.M., Kipfstuhl, S., Drury, M.R., 2017. EBSD analysis of subgrain boundaries and dislocation slip systems in Antarctic and Greenland ice. Solid Earth 8, 883–898. https://doi.org/10.5194/se-8-883-2017

Wilson, C.J.L., Russell-Head, D.S., Sim, H.M., 2003. The application of an automated fabric analyzer system to the textural evolution of folded ice layers in shear zones. Ann. Glaciol. 37, 7–17. https://doi.org/10.3189/172756403781815401